Magnetic, electronic, dielectric and optical properties of Pr(Ca:Sr)MnO_3

J. Sichelschmidt[1,a], M. Paraskevopoulos[2], M. Brando[2], R. Wehn[2], D. Ivannikov[2], F. Mayr[2], K. Pucher[2], J. Hemberger[2], A. Pimenov[2], H.-A. Krug von Nidda[2], P. Lunkenheimer[2], V.Yu. Ivanov[3], A.A. Mukhin[3], A.M. Balbashov[4], and A. Loidl[2]

[1] Max Planck Institute for Chemical Physics of Solids, 01187 Dresden, Germany
[2] Experimentalphysik V, Universität Augsburg, 86135 Augsburg, Germany
[3] General Physics Institute, Russian Academy of Sciences, 105835 Moscow, Russia
[4] Moscow Power Engineering Institute, 105835 Moscow, Russia

Abstract. The charge-ordered perovskite $Pr_{0.65}Ca_{0.28}Sr_{0.07}MnO_3$ was investigated by means of magnetic susceptibility, specific heat, dielectric and optical spectroscopy and electron-spin resonance techniques. Under moderate magnetic fields, the charge order melts yielding colossal magnetoresistance effects with changes of the resistivity over eleven orders of magnitude. The optical conductivity is studied from audio frequencies far into the visible spectral regime. Below the phonon modes hopping conductivity is detected. Beyond the phonon modes the optical conductivity is explained by polaronic excitations out of a bound state. ESR techniques yield detailed informations on the (H,T) phase diagram and reveal a broadening of the linewidth which can be modeled in terms of activated polaron hopping.

PACS. 63.20.-e Phonons in crystal lattices – 71.30.+h Metal-insulator transitions and other electronic transitions – 72.60.+g Mixed conductivity and conductivity transitions – 78.30.-j Infrared and Raman spectra

1 Introduction

The observation of colossal magnetoresistance (CMR) effects in perovskite-manganite films [1] enormously stimulated the research on manganese oxides with perovskite structure. Amongst these systems Ca and Sr doped $PrMnO_3$ revealed the most spectacular effects like a magnetic-field induced metal to insulator transition (MIT) [2], an X-ray [3] and photo induced MIT [4] as well as the observation of a transformation of the insulating (I) into a metallic (M) and ferromagnetic (FM) state as a function of an external electric field [5].

A series of papers [6–8] reported on structural, magnetic, and transport properties of $Pr_{1-x}Ca_xMnO_3$ ceramics for concentrations $0 < x < 1$. The (x,T)-phase diagram shows a high-temperature orthorhombic O phase, which is followed by a Jahn-Teller distorted orthorhombic O' phase for $x < 0.3$ and by a tetragonal phase for $0.3 < x < 0.9$. For Ca concentrations close to 1 the samples remained (O) orthorhombic down to the lowest temperatures. Guided by the early work of Goodenough [9] and Wollan and Koehler [10], an orbitally and charge ordered phase around $x = 0.5$, extending from $x = 0.3$ to $x = 0.7$ has been proposed [6–8]. Two-phase regions were detected close to $x = 0.3$ and $x = 0.9$. The magnetic structure was found to be of A-type at low Ca doping and of CE-type in the charge-ordered state. The Pr moments were found to undergo a ferromagnetic order below 40 K with a relatively small ordered moment [8].

Subsequently, the anomalous magneto-transport properties, including the field induced MIT transition [2,11] and the magnetic structure [12] of $Pr_{1-x}Ca_xMnO_3$ have been investigated in detail. It is now well established that for $0.15 < x < 0.3$ the paramagnetic (P) insulator is followed by a FM and insulating state. For $x > 0.3$ charge-order is established at 240 K followed by an antiferromagnetic (AFM) and insulating state and finally by a canted antiferromagnetic (CA) insulator [11]. The magnetic-field induced transition of the charge-ordered and insulating state to a ferromagnetic and metallic state is of first order and is accompanied by large hysteresis effects, which even remain irreversible at low temperatures [2,11]. In this regime large magneto-resistance effects become apparent which amount approximately ten orders of magnitude [2,11,13]. It has been shown that in zero magnetic field the MIT can be induced by external hydrostatic pressure and also by internal chemical pressure, *e.g.* by substituting Ca by Sr [14,15].

From the published work so far [12,16] the following structural and electronic properties can be deduced for $Pr_{0.7}Ca_{0.3}MnO_3$: At $T_{CO} \approx 200$ K charge and orbital

[a] e-mail: sichelschmidt@cpfs.mpg.de

order is established accompanied by a tetragonal distortion of the lattice. At $T_N \approx 150$ K AFM order of CE type appears which becomes slightly canted below $T_{CA} \approx 120$ K. Here a FM component evolves in addition to the AFM ordering. In the CA phase the results can equally well be explained assuming electronic phase separation into metallic FM and insulating AFM clusters [17]. In finite magnetic fields a metal to insulator transition can be induced which is irreversible at low temperatures ($T < 60$ K) [11]. Optical investigations have been carried out by Okimoto *et al.* [18,19]. From an analysis of the optical conductivity the evolution of a strongly anisotropic gap at low temperatures is reported and closing of the gap with increasing magnetic fields is documented.

In the present work we investigate single crystals of $Pr_{0.65}Ca_{0.28}Sr_{0.07}MnO_3$. *Via* the tolerance factor this composition has been finetuned to reveal the largest magneto-resistance effects. According to the schematic phase diagram of Yoshizawa *et al.* [15] this compound is very close to the phase boundary where a FM and metallic state is established in zero magnetic field. The aim of the present work is to provide a detailed study of a doped $PrMnO_3$ sample, which is close to the metal-to-insulator transition and, hence, is expected to reveal the largest CMR effects. We present electrical resistivity, magnetic susceptibility, magnetization, heat capacity, dielectric permittivity, microwave and optical conductivity, X-band, and high-field ESR results, which reveal fundamental new insights into the physics of the manganites. First of all we found magneto-resistance effects of more than eleven orders of magnitude. We present the frequency dependence of the conductivity and the dielectric constant covering 15 decades in frequency. In analyzing the optical conductivity we focus on both, phonon-like and electronic excitations and try to correlate their temperature dependences with the different structural and electronic phase transitions. And finally we use high-field ESR experiments to study in detail the (H,T)-phase diagram and to gain insight into the (H,T)-space where large irreversibilities occur.

2 Experimental details

Single crystals of $Pr_{0.65}Ca_{0.28}Sr_{0.07}MnO_3$ (PCSMO) were grown by the floating-zone method with radiation heating. Raw Pr_6O_{11}, $SrCO_3$, $CaCo_3$, and Mn_3O_4 chemicals of high purity (not less 99.9%) were used for ceramic-rods preparation. Some excess of Mn_3O_4 concentration (about 0.5%) was used in order to compensate for Mn loss due to an evaporation from the melt in the floating-zone. The initial synthesis of composition was provided by annealing the mixed chemical powders at temperatures about 1200–1300 °C for 24 h. After pressing the feed rods they were sintered at 1350–1400°C for 24 h. The single crystals were grown in an air atmosphere with a growth speed of 7–10 mm/h and a rotation speed of the feed rod about 60 r/min. Crystals with a typical growth direction of [100] have been cut from the main rod to a thickness of 0.5–1 mm and then polished using a 0.25 μm diamond paste. At room temperature X-ray diffraction measurements confirmed the Pbnm orthorhombic structure with $a = 5.431(3)$ Å, $b = 5.4438(22)$ Å, and $c = 7.685(5)$ Å. These parameters indicate the O orthorhombic structure with $c/a \gtrsim \sqrt{2}$ and $a < b$. The ratio $c/(a\sqrt{2}) = 1.0006$ indicates that the PCSMO crystals under investigation are close to the O' orthorhombic structure, characteristic of pure and JT distorted $PrMnO_3$. According to the tolerance factor of $t = 0.918$ clear deviations from the ideal cubic perovskite structure ($t = 1$) are expected.

The magnetic susceptibility and the magnetization were measured using an Oxford AC-susceptometer for temperatures 1.5 K $< T <$ 300 K in fields up to 140 kOe and a Quantum Design SQUID magnetometer (1.5 K $< T <$ 800 K). The DC electrical resistivity and the magnetoresistance have been measured with a standard four-probe technique in an Oxford cryostat and in fields up to 14 T. The temperature-dependent heat capacity was determined with a standard AC method in the same cryostat for temperatures 4.2 K $< T <$ 300 K and using a relaxation method in an Oxford ^{3}He cryostat for 0.3 K $< T <$ 3 K.

The dielectric permittivity and the complex conductivity were recorded using an autobalance bridge (HP4284) from 20 Hz to 1 MHz and an impedance analyzer (HP4291A) from 1 MHz to 1.8 GHz [20]. For these measurements a two-point electrode configuration was used. The microwave conductivity has been measured at 7.3 GHz utilizing a microwave-perturbation technique within a ^{4}He-flow cryostat. Transmission experiments in the frequency range from 30 GHz to 1 THz (1–33 cm^{-1}) were performed utilizing a set of backward-wave oscillators. These measurements were performed in a Mach-Zehnder configuration [21], which allows measurements of transmission and phase shift of the sample. The conductivity and dielectric constant were calculated from the spectra using the exact Fresnel equations for the complex transmission coefficient. The same optical setup with a split-coil magnet (0–80 kOe) was used for the high-field ESR experiments. The ESR measurements at X-band frequencies ($\nu \approx 9$ GHz) were performed with a Bruker ELEXSYS spectrometer.

In the far-infrared, mid-infrared, and visible regime near normal incidence reflectivity spectra, $R(\nu)$, were measured with Bruker rapid-scan Fourier spectrometers. The sample was placed in the exchange gas of a ^{4}He-bath cryostat allowing for temperatures 5 K $\leq T \leq$ 300 K. For detection GaP and Si diodes, a MCT (HgCdTe) detector and a doped-Si-Bolometer were employed to cover frequencies between 40 cm^{-1} (5 meV; 1.2 THz) and 42 000 cm^{-1} (5.2 eV; 1260 THz). The optical conductivity spectra, $\sigma'(\nu)$, were calculated from $R(\nu)$ by a Kramers-Kronig (KK) transformation. In order to perform a KK transformation, the $R(\nu)$ data have to be extrapolated towards zero and infinite frequencies. Fortunately, in the present work conductivity and dielectric constant data extending down to frequencies as low as 20 Hz are available, which can be used for a proper low-frequency

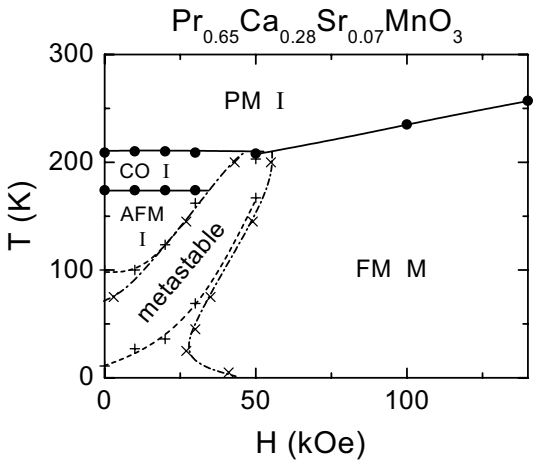

Fig. 1. (H,T) phase diagram of PCSMO determined by resistivity, magnetic susceptibility and magnetization results. The metastable region is marked by hysteretic effects. Changing the field at constant temperature (×, dash-dotted lines) or increasing the temperature at constant magnetic field (+, dashed lines) leads to a variation of the extend of this region.

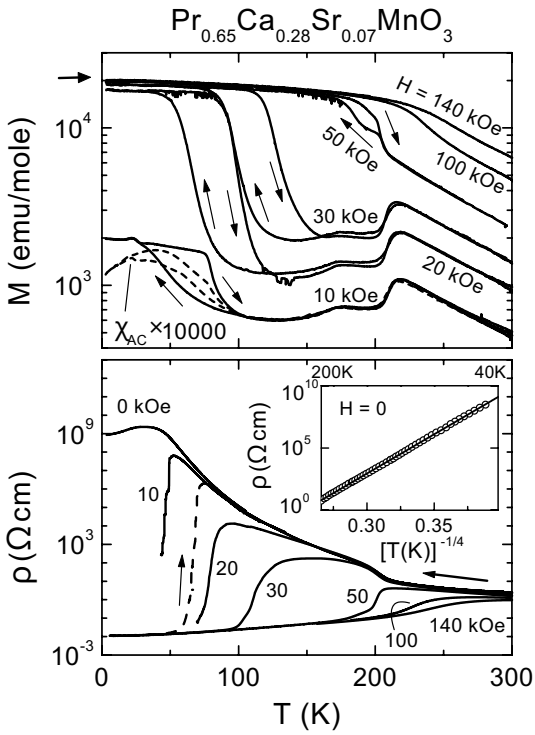

Fig. 2. Upper frame: Temperature dependence of the magnetization (solid lines) for various external magnetic fields. The dashed line shows the magnetic AC susceptibility (multiplied by a factor of 10^4) taken at zero external field using a frequency of $\nu = 1000$ Hz and a field of $H_{\mathrm{AC}} = 0.2$ $\mathrm{Oe_{rms}}$. The theoretical value for the saturation magnetization, $M_{\mathrm{S}} \approx 3.65\,\mu_{\mathrm{B}}$, is indicated by an arrow. Lower frame: Temperature dependence of the DC resistivity for various external magnetic fields (same as in upper frame). The solid lines were taken upon cooling. The dashed line represents results in zero magnetic field on heating after applying 50 kOe at low temperatures for a few minutes. The inset shows the resistivity at zero magnetic and a constant electric field in a representation leading to a linear behavior for VRH (see text). The line was calculated with $T_0 = 4.4 \times 10^8$ K.

extrapolation. Therefore the significance of the present results on $\sigma'(\nu)$, especially in the far-infrared region, is substantially enhanced compared to earlier work were rather crude assumptions had to be made for the low-frequency extrapolation. For frequencies above 42 000 cm^{-1}, $R(\nu)$ was approximated using the reflectivity data of $LaMnO_3$ (Ref. [22]) up to 2.4×10^5 cm^{-1} and then was extrapolated to zero with a ν^{-4} power law.

3 Results and discussion

3.1 (H,T)-phase diagram

Figure 1 shows the (H,T)-phase diagram of the PCSMO sample under investigation. This phase diagram has been determined in the series of experiments which will be documented below, however similar phase diagrams have been published by a number of authors [11,23]. In zero external magnetic field the crystal passes through a series of phase transitions. Starting from room temperature and with decreasing temperature, at $T_{\mathrm{CO}} \approx 210$ K the sample undergoes a structural phase transition between two different insulating paramagnetic phases. In the phonon spectra (Sect. 3.5.2) a shift of the eigenfrequencies and the appearance of satellite excitations are a clear indication of a lowering of the symmetry and probably of a doubling of the unit cell. In neutron diffraction experiments [15,24] this phase was identified as a charge-ordered (CO) state. On further cooling, the crystal undergoes an AFM phase transition ($T_{\mathrm{N}} \approx 170$ K) and at $T_{\mathrm{irr}} \approx 100$ K a transition into a canted or a mixed phase can be assumed. At this latter temperature strong irreversibilities (hysteresis effects, irreversibilities under applied magnetic fields) evolve which become increasingly stronger at low temperatures. The range of the irreversibilities is indicated in Figure 1 by the dashed and dash-dotted lines. It is straightforward to assume that these irreversibilities are introduced by phase separation processes, most likely of FM clusters within an AFM background. And indeed, with an applied external field the system transforms into a FM metal, which for fields larger than 50 kOe is stable almost up to room temperature.

3.2 Susceptibility and magnetization

Figure 2 shows the magnetization (solid lines in the upper frame) and the resistivity (lower frame, measured at constant current) for various external fields up to 140 kOe as a function of temperature. In addition the zero-field AC susceptibility is indicated (dashed lines in the upper frame). In the curves corresponding to $H < 100$ kOe the structural phase transition at 210 K can be well identified and the magnetization curves show hysteretic

behavior (indicated by arrows in the upper frame of Fig. 2). For $H = 20$ kOe and $H = 30$ kOe a small hysteresis of the magnetization extends up to 200 K. The AFM phase transition at $T_N \approx 170$ K is visible in the magnetization and susceptibility. According to published data [8], the small anomaly in $M(T)$ and in $\chi_{AC}(T)$ at 10 kOe close to 25 K could be ascribed to the onset of antiferromagnetic order of the praseodymium ions. However, the onset of magnetic order of the Pr^{3+} at 25 K is rather unlikely taking into account the weak Pr-Pr interactions in perovskite-like compounds. In addition, as will be discussed later, no anomaly could be detected in the heat capacity $C(T)$ close to 25 K. But of course the FM component of the ordered manganese spins certainly will polarize the praseodymium moments. The saturation value of the magnetization M_S at high fields and low temperatures agrees well with the theoretical value $M_S \approx 3.65\,\mu_B$ expected for 0.65 Mn^{3+} and 0.35 Mn^{4+}. No additional contribution from Pr^{3+} can be detected. At the same time an effective moment of $\mu_{eff} \approx 5.35\,\mu_B$ is evaluated from the reciprocal susceptibility up to 800 K (not shown), which is clearly higher than the manganese-only expectation ($\mu_{eff}(\mathrm{Mn}) = 4.57\,\mu_B$). However, including Pr^{3+} moments one expects $\mu_{eff}(\mathrm{Mn,Pr}) = 5.4\,\mu_B$. Therefore at high temperatures the magnetization can only be explained taking the Pr^{3+} moments into account whereas they do not contribute at all at low temperatures. This fact can be explained in two ways: i) it confirms the AFM order of Pr^{3+} at low temperature, or ii) the crystal-field splitting of the ground-state multiplet results in a considerable reduction of the Pr magnetization.

In zero magnetic field $\varrho(T)$ continuously increases on decreasing temperatures (lower frame of Fig. 2). A small step-like increase close to 210 K indicates the CO transition. The slight decrease towards the lowest temperatures may signal a reduction of spin-disorder scattering by the Pr moments. However, electric-field dependences of $\varrho(T)$ (Ref. [5]), which start to play a role below about 70 K, may contribute to this decrease.

When applying an external magnetic field the magnetization increases by about a factor of ten and the resistivity is reduced by more than eleven orders of magnitude. If, at low temperatures, the field is switched off, the sample remains ferromagnetic up to approximately 70 K (dashed line in lower frame of Fig. 2). On further heating it recovers the antiferromagnetic state and then reversibly follows the cooling measurements in zero-field up to elevated temperatures. Above approximately 50 kOe, the PM and insulating state immediately transforms into a FM and metallic state without the transition into the CO insulating state. It is clear however, that the metallic state is that of a "bad" metal at best. The inset in the lower frame of Figure 2 shows resistivity data taken in zero magnetic field under constant voltage, plotted as $\log \varrho(T^{-1/4})$ in order to verify the variable range hopping (VRH) prediction, $\varrho = \varrho_0 \exp(T_0/T)^{1/4}$. The linear behavior clearly demonstrates, that the DC transport properties are dominated by VRH in the CO/I as well as in the AFM/I state.

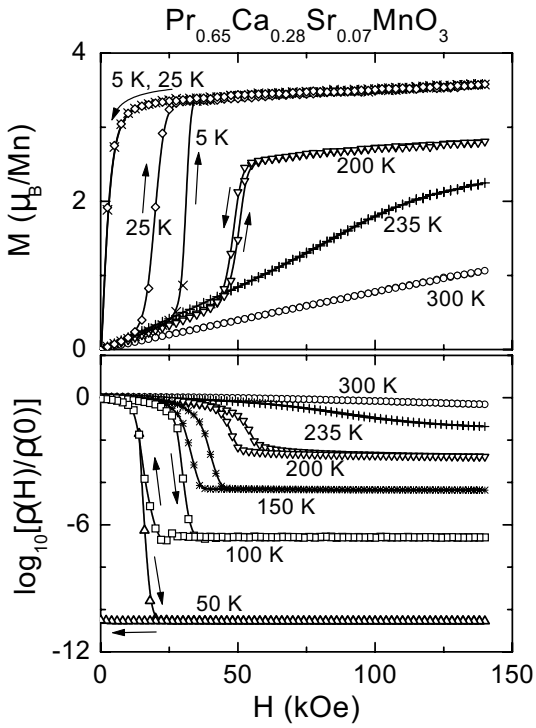

Fig. 3. Magnetic field hysteresis loops of magnetization and resistivity for various temperatures.

The value of $T_0 = 4.4 \times 10^8$ K is of similar magnitude as observed in other manganites [25].

Figure 3 shows field-dependent hysteresis measurements up to 140 kOe of the magnetization (upper frame) and magnetoresistance ϱ/ϱ_0 (lower frame) for various temperatures. At 300 K the magnetization shows a linear field-dependence as can be expected for a paramagnetic state and there is only a minor influence on the resistivity. At $T = 235$ K, just above the CO transition, the increase of the slope with field is indicative of a metamagnetic behavior, which develops concomitant with distinct magnetoresistance effects. But in this temperature regime no hysteresis phenomena can be detected. Below T_{CO} the magnetization as well as the resistivity curves exhibit marked hysteresis loops which significantly broaden on decreasing temperature. At low temperatures the CMR effect reaches enormous values and the resistivity can be changed by eleven orders of magnitude by applying an external magnetic field. The critical field H_{c1}, at which the FM metallic state is induced, decreases for decreasing temperatures and reaches a minimum close to $T \approx 25$ K, but increases again on further decreasing temperatures. The field H_{c2}, at which the insulating state is reestablished is continuously lowered with decreasing temperatures. H_{c2} reaches zero at $T \approx 70$ K. Below that temperature the induced FM metallic state reveals a significant metastability (see curve at 50 K in the lower frame of Fig. 3). In spite of the persistence of the field-induced metallicity at low temperatures the macroscopic magnetization vanishes with lowering the applied field towards zero. This behavior can be explained by domain alignments as also observed

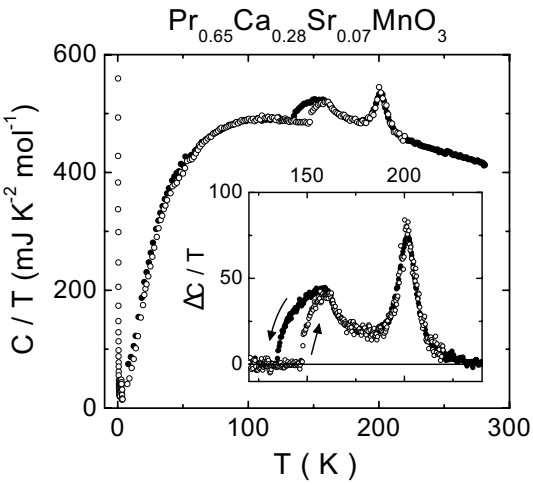

Fig. 4. C/T *vs.* T for $H = 0$ T on cooling (•) and heating (∘). The inset shows $\Delta C/T$ *vs.* T after subtraction of a smooth background.

in soft magnetic materials. The microscopic state is still FM and conducting due to percolating conducting paths.

3.3 Heat capacity

The heat capacity was measured on cooling and heating (0.2 K/min) the sample in zero external magnetic field for temperatures $0.3 \leq T \leq 280$ K (see Fig. 4). We observe the onset of a sharp peak at $T_{\mathrm{CO}} \approx 210$ K corresponding to the charge-ordering transition and a broad anomaly at $T_{\mathrm{N}} \approx 160$ K which indicates the onset of antiferromagnetic order. No thermodynamic anomaly could be detected at $T_{\mathrm{irr}} \approx 100$ K. In addition, no anomaly was detected at 25 K, where the onset of AFM order of the Pr moments has been proposed [8]. The inset of Figure 4 shows the two anomalies after the subtraction of a smooth background. The two transition temperatures are close and the two peaks overlap: the entropy of the two anomalies can be calculated according to $\Delta S = \int(\Delta C/T)\mathrm{d}T$, estimating the integrated entropies ΔS_1 and ΔS_2 for the CO and the AFM transitions, respectively. On cooling the sample we obtain values of $\Delta S_{1\mathrm{down}} = 1.272\ \mathrm{J\,K^{-1}\,mol^{-1}}$ for the CO anomaly and $\Delta S_{2\mathrm{down}} = 1.388\ \mathrm{J\,K^{-1}\,mol^{-1}}$ for the AFM one. On heating the entropy for the charge ordering transition changes slightly to $\Delta S_{1\mathrm{up}} = 1.231\ \mathrm{J\,K^{-1}\,mol^{-1}}$ which is well within the experimental uncertainties. In the AFM region a clear hysteresis is observed and the entropy decreases by more than 30% ($\Delta S_{2\mathrm{up}} = 0.946\ \mathrm{J\,K^{-1}\,mol^{-1}}$). The amount of the entropy associated with the two transitions agrees well with previous measurements performed on this class of materials [26,27] and the AFM entropy is very small compared to the expected value ($\approx$ 12.7 $\mathrm{J\,K^{-1}\,mol^{-1}}$) for the residual spin-entropy. It seems that a fairly large spin-entropy fraction is lost at lower temperatures. In fact, although the transport measurements show an insulating behavior down to the lowest temperature, the Sommerfeld coefficient, extracted from

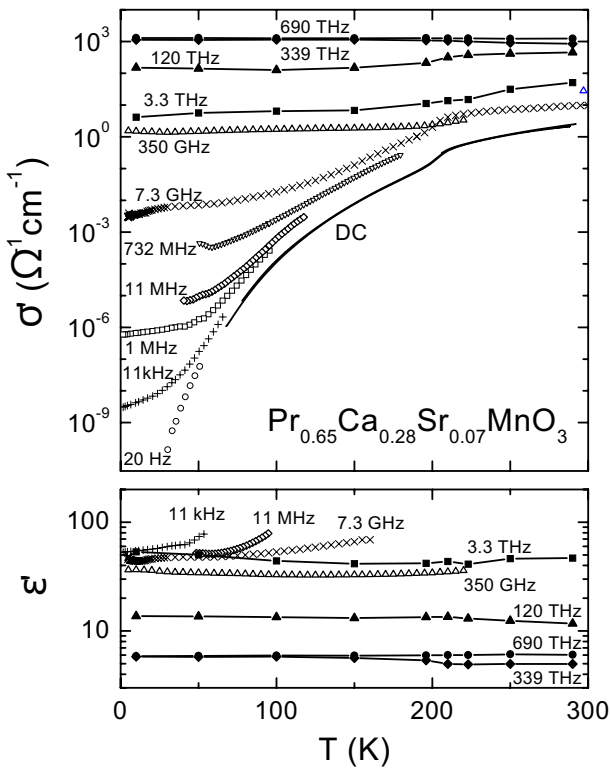

Fig. 5. Temperature dependence of the conductivity σ' and dielectric constant ε' for selected frequencies, combining the results from different experimental setups. Only data points are shown where electrode contributions can be excluded [28]. The solid line shows the result of a fourpoint DC experiment. For $\nu > 1$ THz the data points are connected by lines.

the low-temperature data, $\gamma \approx 18.24\ \mathrm{mJ\,K^{-2}\,mol^{-1}}$, is large. Probably this large γ value is not due to conduction electrons within the metallic regions but results predominantly from low-lying magnetic excitations. Below 1 K, Mn-hyperfine contributions to the heat capacity are observed [26], leading to a T^{-2} increase towards low temperatures. It is caused by the large local magnetic field at the Mn nuclei due to electrons in unfilled shells. The local magnetic field at the Mn nuclei can be calculated from the slope of the T^{-2} increase and we obtain $H_{\mathrm{Hyp}} = 5.82 \times 10^7$ A/m [27]. This value agrees well with that reported by Ramirez *et al.* [27] for a similar composition and it is about three times larger than the values of other manganites which we have previously investigated. A detailed analysis and heat capacity measurements in external magnetic fields will be published elsewhere.

3.4 Dielectric results

The temperature dependence of the conductivity and of the dielectric constant is shown in Figure 5 for a variety of measuring frequencies, spanning the exceptionally broad range of 20 Hz to 690 THz. In this figure we only include results which are not affected by electrode contributions, which become important for frequencies $\nu < 1$ GHz and

high temperatures (see below). Focusing on the conductivity (upper frame), at high temperatures all AC conductivity curves with $\nu \leq 350$ GHz join a common curve, which thereby can be identified as the DC conductivity. Indeed it is paralleled by the DC conductivity, measured by a standard 4-point technique (solid line). For lower temperatures a significantly weaker temperature dependence is observed and a strong frequency dependence shows up, typical for hopping conductivity. Taking into account the detected VRH behavior of the DC conductivity (inset of Fig. 2), it can be stated that both, DC and AC charge transport (the latter at least for $\nu \leq 350$ GHz), in $Pr_{0.65}Ca_{0.28}Sr_{0.07}MnO_3$ are dominated by hopping of localized charge carriers. In the THz regime the temperature dependence is weak, but still visible. It is interesting to note that, on increasing temperature, the conductivity still increases for measuring frequencies of 120 THz. Only at frequencies as high as 690 THz the conductivity remains constant as a function of temperature. We would like to recall that 690 THz corresponds to approximately 35 000 K in temperature, which is about hundred times the thermal energy. The dielectric constant increases with decreasing frequency, saturating at a value of the order of 50 at intermediate frequencies. The onset of an increase of $\varepsilon'(T)$, seen at the lowest frequencies in Figure 5 can be attributed to contributions of hopping conductivity to the imaginary part of the conductivity as explained below.

Figure 6 presents the frequency dependence of the conductivity (upper panel) and the dielectric constant (lower panel) [28]. For 100 K we show the curve down to the lowest frequency of 20 Hz. The steplike increase of $\sigma'(\nu)$ at about 100 kHz and the huge values of ε' at low frequencies can be attributed to the formation of capacitive contact layers between the semiconducting sample and the metallic contacts. A more detailed analysis of this behavior with an equivalent circuit involving the sample impedance, connected in series to a lossy capacitor for the contacts (see, *e.g.*, Ref. [29]), is given in reference [28]. At sufficiently high frequencies (*e.g.* at $\nu > 1$ MHz for 100 K) the contact capacitance becomes effectively shorted and the intrinsic sample response is detected. The curves shown in Figures 5 and 6 (except for 100 K) have been restricted to regions where electrode contributions can be neglected.

Towards low frequencies all $\sigma'(\nu)$ curves, except that for 5 K, start to saturate, which can be attributed to the approach of the DC regime. With increasing temperature the DC plateau increases and the crossover to the AC regime shifts to higher frequencies. It is remarkable that at room temperature the DC regime seems to extend nearly up to the phonon modes at THz frequencies. At higher frequencies σ' shows a smooth transition to a power law $\sigma' = \sigma_1 \nu^n$, with $n \approx 1.13$ and for the lowest temperatures this power law can be observed over the extraordinary broad frequency range of nearly 10 decades. The approach of such a nearly linear increase of $\sigma'(\nu)$ (corresponding to a nearly constant dielectric loss, $\varepsilon'' \sim \sigma'/\nu$) for high frequencies was found in a variety of materials (*e.g.*, Refs. [30–35]), including $La_{1-x}Sr_xMnO_3$ with small x [30], and was termed "second universality" [32]. The development of a microscopic understanding of this phenomenon is still in its beginning stages, with some explanations been proposed mainly for amorphous ionically conducting materials (*e.g.*, Ref. [34]). A *sublinear* increase, $\sigma'(\nu) = \sigma_0 \nu^s$, $s < 1$, is predicted by various models for hopping conductivity of localized charge carriers [36]. Such a behavior, termed "universal dielectric response" (UDR) [31], was also found in low-doped $La_{1-x}Sr_xMnO_3$ [30]. However, theses models cannot explain the second universality behaviour, *i.e.* a *superlinear* increase of $\sigma'(\nu)$. It seems reasonable that the UDR and the second universality behavior, which often are observed simultaneously in the same material [30, 32–35], are separate physical phenomena. Indeed, a closer analysis [28] of the crossover of $\sigma'(\nu)$ from DC to the ν^n power law in the present data reveals that it is too smooth to be described by the simple ansatz $\sigma' = \sigma_{DC} + \sigma_1 \nu^{1.13}$. This indicates the additional presence of a UDR contribution also in PCSMO, leading to $\sigma' = \sigma_{DC} + \sigma_0 \nu^s + \sigma_1 \nu^{1.13}$.

For the imaginary part of the conductivity, obtained by the Kramers-Kronig transformation, the UDR leads to

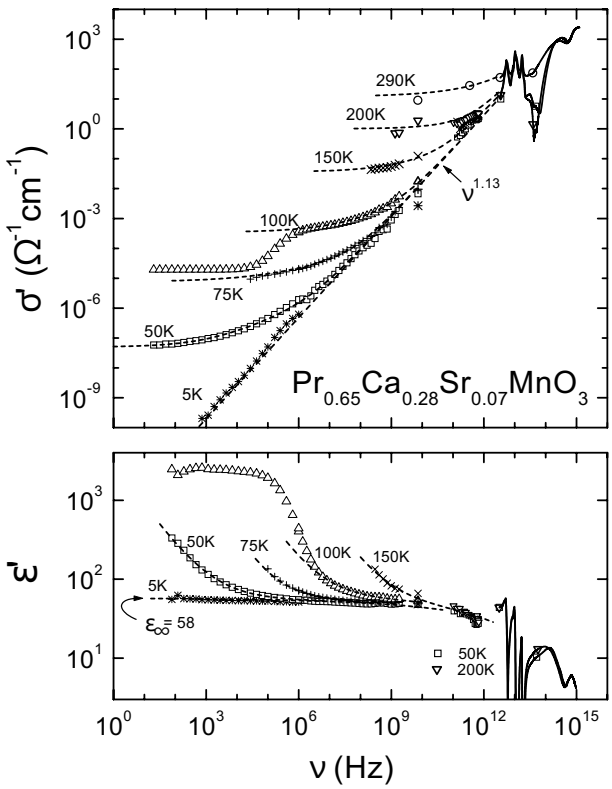

Fig. 6. Frequency dependence of the conductivity σ' and dielectric constant ε' in the whole investigated frequency range for selected temperatures. Except for 100 K, only data points are shown where electrode contributions can be excluded [28]. For $\nu > 1$ THz the results are presented as solid lines with two symbols per curve identifying the temperature. The dashed lines are fits combining a DC contribution, a hopping conductivity contribution, a $\nu^{1.13}$ power law, and a limiting high-frequency dielectric constant ε_∞, performed simultaneously for σ' and ε' (for details, see Ref. [28]).

$\varepsilon' \sim \sigma''/\nu \sim \nu^{1-s}$ [31]. In addition, the second universality causes a term $\varepsilon' \sim -\nu^{n-1}$ and finally ε_∞ has to be taken into account, covering the ionic and electronic polarizability. The dashed lines in Figure 6 are fits with a combination of the above-mentioned contributions, performed simultaneously for $\sigma'(\nu)$ and $\varepsilon'(\nu)$. A satisfactory description of both quantities well up to the phonon modes is achieved [28]. The analysis of the data reveals that the ν^s contribution, often ascribed to hopping processes, plays a role up to extraordinary high frequencies around THz. Details on the resulting fitting parameters are given in reference [28]. Here we only want to mention that the frequency exponent s seems to be somewhat smaller than the prediction of the VRH model, $s \approx 0.8$, possibly indicating polaronic hopping. In addition, we want to point out the rather high value of $\varepsilon_\infty \approx 58$ indicated in the lower frame of Figure 6.

In the phonon region the $\nu^{1.13}$ and ν^s power laws may be suspected to lead to a background conductivity at low and high temperatures, respectively. At frequencies above the phonon modes, a qualitative change of behavior is observed and the regime of photon-induced electronic interband and intraband transitions is entered, which will be discussed in detail below.

3.5 Optical properties

3.5.1 Electronic excitations

We now turn to the optical conductivity. Figure 7 shows the conductivity *vs.* wavenumber for photon energies up to 5 eV. The conductivity has been measured as a function of temperature below 4 eV and for higher energies at room temperature only. The characteristic feature of correlated electron systems, an extreme shift of spectral weight reaching up to energies as high as 2 eV is clearly observed. This shift of spectral weight can most easily be explained by polaronic excitations which may be related to a dynamic Jahn-Teller effect. Most probably these excitations are due to Mn^{3+} to Mn^{4+} interband transitions [37]. The peak at 4.8 eV is a charge-transfer transition from the oxygen p-orbitals to the manganese e_g states [22] and has been observed in a number of doped manganites [38].

The peak located at about 1.2 eV is more difficult to explain. In the Jahn-Teller distorted phase of pure and insulating $LaMnO_3$ a peak is observed at 1.89 eV and has been interpreted as a transition between the Jahn-Teller split e_g bands [22]. These transitions are dipole forbidden but would get finite intensities *via* a mixing with the oxygen p-orbitals. Later on, in the doped compounds the feature near 1 eV in the PM and I phases has been explained by Quijada *et al.* as intersite e_g transitions [38]. It is also our belief that the transition close to 1 eV as shown in Figure 7 represents an excitation of an e_g electron out of a bound state (local distortion around a Mn^{3+} site) to a neighboring Mn^{4+} site. This transition clearly represents an excitation closely related with a dynamic Jahn-Teller effect.

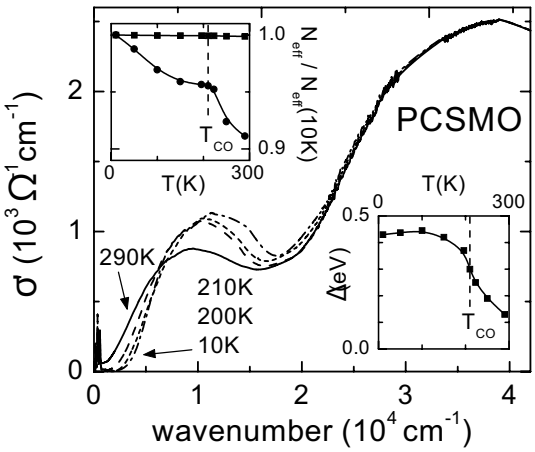

Fig. 7. Energy dependence of the optical conductivity σ' for various temperatures. The upper inset shows the temperature dependence of the normalized spectral weight which was obtained by integrating $\sigma'(\nu)$ between either 0–23 000 cm^{-1} (squares) or 750–23 000 cm^{-1} (circles). The lower inset shows the temperature dependence of the onset Δ of the polaron excitation peak located at $h\nu \approx 1.2$ eV.

At first sight it becomes clear that with decreasing temperature the maximum shifts to higher energies and the width slightly decreases. The latter behavior can be expected in the case of small-polaron absorption [39], which is significantly phonon broadened on increasing temperature. The maximum of the absorption corresponds to two times the polaron binding energy. At room temperature the polaron excitation peak is centered at about 1.2 eV and has an onset $\Delta = 0.14$ eV. The onset energy has been derived using a linear extrapolation as was proposed by Okimoto *et al.* [19]. The lower inset of Figure 7 shows the temperature dependence of this lower bound of the polaron band. Δ significantly increases at $T_{CO} = 210$ K and saturates at a value of 0.45 eV at lower temperatures. The upper inset of Figure 7 shows the temperature dependence of the spectral weight N_{eff} which can serve as a measure of the kinetic energy of charge carriers. The optical weight remains constant if summed up for frequencies up to 23 000 cm^{-1}, including the phonon regime (squares). If the phonon regime is omitted (750–23 000 cm^{-1}, circles), a significant fraction of the spectral weight is lost at elevated temperatures. This effect is strongly enhanced at the structural phase transition T_{CO}. From this it becomes clear that a significant part of the spectral weight as observed in the phonon regime at high temperatures becomes shifted to higher frequencies as the gap value increases. Using handwaving arguments it seems likely, that when the polaron band starts to leak into the phonon regime the "electronic" background underneath the phonons becomes clearly enhanced.

3.5.2 Phonon properties

The phonon bands of PCSMO are documented in Figure 8. The main three bands are located approximately at 185,

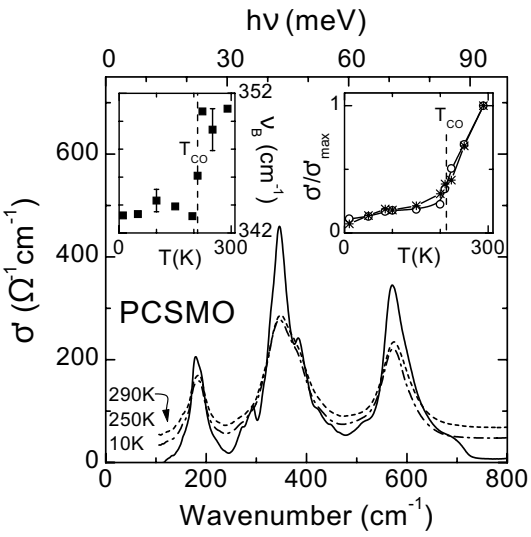

Fig. 8. Energy dependence of the optical conductivity σ' for three temperatures focusing on the phononic part of excitations. The left inset shows the temperature dependence of the frequency ν_{B} of the internal bending vibration. The right inset shows the temperature dependence of the normalized $\sigma'(\nu)$ for $\nu_1 = 120$ cm^{-1} (stars) and $\nu_2 = 750$ cm^{-1} (circles).

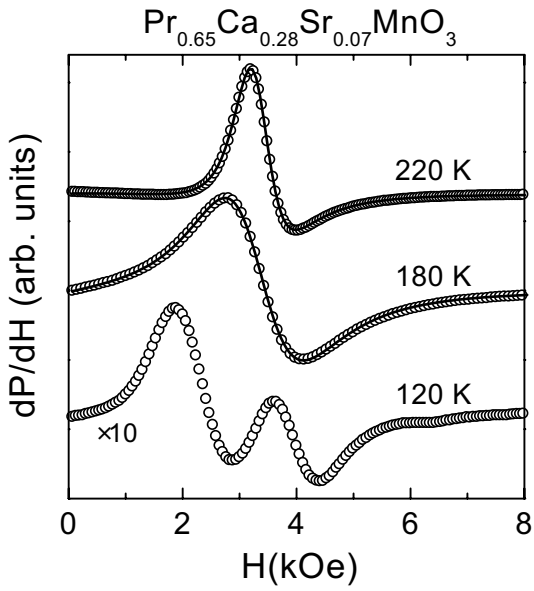

Fig. 9. ESR spectra ($\mathrm{d}P/\mathrm{d}H$, P: absorbed power) at three temperatures. The solid lines represent fits with a Dysonian line shape.

350, and 575 cm^{-1} close to the values which are expected for cubic ABO_3 systems [40]. These three bands correspond to the external vibration of the A cations against the BO_6 octahedra, to a bending and to a stretching mode, respectively. Clearly the bending mode is asymmetrically broadened at room temperature due to the orthorhombic distortion of the lattice. At room temperature the phonon bands are located above a broad background, which most probably is of electronic origin. To provide experimental evidence for this behavior, the right inset of Figure 8 shows the temperature dependence of normalized $\sigma'(\nu, T)$ for $\nu_1 = 120\,\mathrm{cm}^{-1}$ (stars) and $\nu_2 = 750\,\mathrm{cm}^{-1}$ (open circles). Both, $\sigma'(\nu_1, T)$ and $\sigma'(\nu_2, T)$ exhibit the same temperature dependence with a clear change of slope at T_{CO}. It seems that electronic and magnetic degrees of freedom strongly mix with the phonon modes and yield a broad hump-like intensity, which peaks in the phonon regime. Similar results have been observed in a number of systems, but so far we are not aware of any sound theoretical explanation. Naively one might expect that due to a strong electron-phonon coupling the adiabatic approximation breaks down. Above 210 K the electronic background strongly increases (right inset). Below $T_{\mathrm{CO}} \approx 210$ K new phonon modes appear which indicate that the crystal symmetry is lowered or that the unit cell is doubled. Significant side bands appear close to 290, 380, 510, and 700 cm^{-1}. Lattice dynamical calculations are needed to identify these modes in the low temperature structure.

To provide a more qualitative analysis we fitted the phonons using a sum of Lorentz-oscillators. A correct analysis is hampered by the fact that some modes split and broaden at the same time. Nevertheless our analysis yields significant shifts of the eigenfrequencies at the structural phase transition. As a representative result, the left inset of Figure 8 shows the temperature dependence of the frequency ν_{B} of the internal bending vibration, revealing a step-like decrease of approximately 2% at T_{CO}.

3.6 Electron spin resonance (ESR)

3.6.1 X-band measurements

ESR probes the absorbed power of a transversal magnetic microwave field as a function of the static magnetic field H. To improve the signal-to-noise ratio, a lock-in technique is used by modulating the static field, which yields the derivative of the resonance signal $\mathrm{d}P/\mathrm{d}H$. Figure 9 shows three representative resonance signals, for $T < T_{\mathrm{N}}$ ($T = 120$ K), for $T_{\mathrm{N}} < T < T_{\mathrm{CO}}$ ($T = 180$ K), and for $T > T_{\mathrm{CO}}$ ($T = 220$ K). Below T_{N} the spectra contain several lines which exhibit a complicated dependence on temperature and crystal orientation. This behavior is a signature of magnetic ordering in this temperature regime and will not be treated in the further discussion.

Above T_{N} the resonance lines are well fitted with a Dysonian line shape [41]. A broad and symmetric ESR line, as observed for 180 K, signals an insulating state close to magnetic order. When crossing the phase-transition temperature T_{CO} the temperature dependence of the conductivity is clearly reflected in the asymmetry of the line shape. Due to a significant increase of the conductivity at $T > T_{\mathrm{CO}}$ (see lower frame of Fig. 2) the penetration depth gets smaller than the sample size. Therefore the ratio of dispersion to absorption is changed and the signal appears more asymmetric. Similar asymmetric ESR-lines were also observed in (La:Sr)MnO_3 [42].

The resonance signals depend only weakly on crystal orientation in the static magnetic field. This is expected

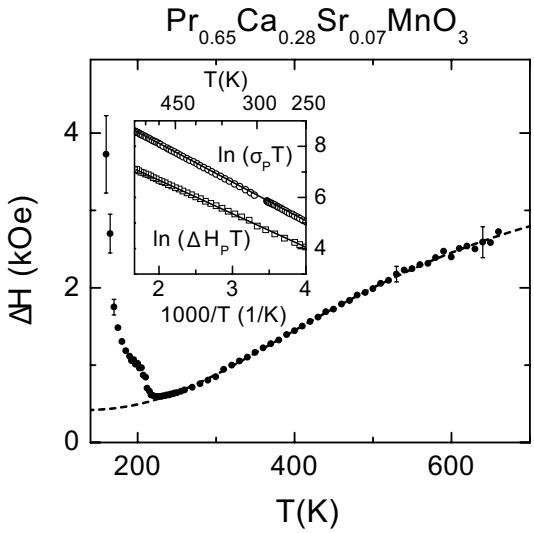

Fig. 10. Temperature dependence of the ESR linewidth ΔH (HWHM). The dashed line fits the high temperature part of ΔH with equation (1). The inset demonstrates the similarity of the temperature dependences of linewidth and DC conductivity. Here the polaron hopping contributions $\Delta H_{\rm P} = \Delta H - \Delta H_0$ and $\sigma_p = 1/(\varrho - \varrho_0)$ are shown ($\Delta H_0, \varrho_0$: residual linewidth and resistivity). The axes are scaled such that the second term of equation (1) appears linear. The solid lines are linear fits demonstrating the applicability of equation (1).

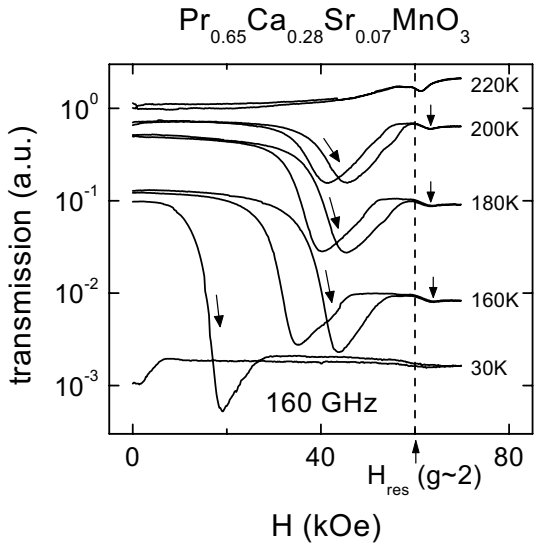

Fig. 11. High-field ESR transmission spectra at various temperatures and at an incident radiation with $\nu = 160$ GHz (5.34 cm^{-1}).

for crystals close to cubic symmetry. The anisotropy of the linewidth amounts to 2.5% which is ten times smaller than in slightly doped (La:Sr)MnO_3 exhibiting the Jahn-Teller distorted O' phase [42]. The anisotropy of the resonance field is temperature dependent and reaches its largest value of 1.8% at $T = 220$ K, close to $T_{\rm CO}$. The g-factor which is determined by the resonance field is close to the free-electron value of 2. A strong temperature dependence of the g-factor is observed close to the antiferromagnetic ordering temperature $T_{\rm N}$, indicating a distribution of internal magnetic fields.

Figure 10 shows the temperature dependence of the linewidth ΔH. On cooling, at the phase transition temperature $T_{\rm CO}$ a step-like increase of the linewidth is observed. This could be due to either changes in the crystal field or to an increase of the antisymmetric Dzyaloshinsky-Moriya interaction. The latter is commonly observed in the La-based manganites [42]. With further decreasing the temperature towards the antiferromagnetic ordering temperature $T_{\rm N} \approx 170$ K the linewidth strongly increases, indicating increasing antiferromagnetic spinfluctuations in addition to inhomogeneous static fields.

For temperatures $T > T_{\rm CO}$, $\Delta H(T)$ increases and can well be described using

$$\Delta H = \Delta H_0 + \frac{A}{T} \exp(-E_a/k_{\rm B}T) \qquad (1)$$

with $\Delta H_0 = 820$ Oe, $A = 2.1 \times 10^7$ Oe K, and $E_a = 0.11(0)$ eV. The second term results from the conductivity due to thermally activated hopping of adiabatic small polarons [43] which determines the ESR linewidth *via* the so called bottleneck spin-lattice relaxation which is found in a variety of Mn- and Cu-oxide systems [44,45]. The spin resonance is due to the strongly coupled t_{2g}–e_g-spin system of the Mn^{3+}/Mn^{4+} ions and the hopping of the e_g electrons broadens the ESR-line *via* spin-orbit coupling. The proportionality between corrected DC conductivity and ESR-linewidth in the paramagnetic and insulating state is demonstrated in the inset of Figure 10. Both quantities can be well described by a hopping motion of small polarons with similar values of activation energy, $E_{\Delta H} = 0.11$ eV and $E_\sigma = 0.13$ eV. Astonishingly these values show a reasonable agreement with the onset of polaronic conduction at $\Delta \approx 0.14$ eV, determined by optical spectroscopy at room temperature (see Sect. 3.5.1 and lower inset of Fig. 7).

3.6.2 High-frequency ESR results

Figure 11 shows the high-field ESR transmission spectra of PCSMO for a frequency $\nu = 160$ GHz. These results can be interpreted as high-field ESR spectra, but also as optical conductivity experiments at submillimeter wavelengths as a function of temperature and an external magnetic field. The transmission is directly proportional to the resistivity. This can be easily verified by comparing Figure 11 with the lower frame of Figure 3 ($\log \varrho$ *vs.* H). When entering the hysteresis regime (see Fig. 1) the transmission drops significantly. Two significant differences show up: i) the effects as observed in the transmission are rather small and amount only two orders of magnitude at 30 K, compared to a decrease of the resistivity over eleven decades. This can be explained by the exponential decrease of the DC conductivity as a

function of temperature, while the submillimeter conductivity reveals a moderate decrease only (see upper frame of Fig. 5), *i.e.* it is already rather high, even without the application of a magnetic field. ii) in the hysteresis regime the transmission becomes very small and increases again when entering the metallic and ferromagnetic state. These effects probably are due to magnetic resonance or Faraday rotation effects when the FM state is established. Further investigations using polarized light are necessary to elucidate this behavior in more detail.

In addition, a weak ESR-line can be detected in the transmission spectra of PCSMO. The value of the resonance field is indicated by arrows in Figure 11. For temperatures $T = 220$ K the line is observed close to a resonance field $H_{\rm res} = 60$ kOe corresponding to a g-factor $g \approx 2$. In the PM state $g \approx 2$ is expected for a spin-only system. For temperatures $T \leq 200$ K and magnetic fields $B > 40$ kOe the sample is in the ferromagnetic state. In the FM state the line represents the ferromagnetic resonance (FMR) mode. For the present experiments the static magnetic field was oriented perpendicular to the plane-parallel sample plate. For this geometry the FMR mode is expected to be shifted to higher fields proportional to the spontaneous magnetization ($B_{\rm res} = B_0 - M_{\rm s}$), where B_0 is the resonance field in the paramagnetic state.

4 Summary and conclusions

The present investigation documents an extensive study of magnetic, electrical, optical, and thermodynamic properties of $Pr_{0.65}Ca_{0.28}Sr_{0.07}MnO_3$, a substance which has been fine-tuned to exhibit giant magnetoresistive effects. The combination of the results of this rich variety of experimental techniques allowed for a detailed investigation of the (H,T) phase diagram of this material. A rather complex sequence of PM/I, CO/I, AFM/I, and finally a metastable state at zero external magnetic field is revealed. Beyond 50 kOe the PM and I phase directly transforms into a FM and metallic state close to 200 K. The magnetization and the magnetoresistance have been studied in detail. If FM is induced below 50 K, this phase is stable even at zero field and low temperatures. The resistivity drops by 11 orders of magnitude in fields of 10 kOe. We would like to recall that this enormous CMR effect is observed in a sample exactly at the border between a ferromagnetic and insulating state characterized by charge order. Under finite external magnetic fields the charge order melts, yielding a FM and metallic ground state.

In addition detailed information on the AC conductivity and the dielectric constant is provided, covering the extremely broad frequency range of 14 decades. The DC and AC conductivity at frequencies below the phonon regime reveal the clear signature of hopping transport of localized charge carriers which seems to play a role even in the phonon regime. A rather large high-frequency dielectric constant of $\varepsilon_\infty \approx 58$ was detected. The phonon region was investigated in detail showing clear signatures of the CO phase transition. The phonon modes reveal significant shifts at $T_{\rm CO}$. In addition new modes are observed indicating the lowering of the crystal symmetry and most probably also the doubling of the unit cell. A strong background of electronic origin is observed below the phonon modes when the polaron absorption is shifted towards the phonon frequencies.

Beyond the phonon frequencies the optical conductivity data reveal the characteristic features of small polaron absorption with a typical binding energy of around 0.6 eV. The binding energy increases at the transition into the CO state. We interpret this absorption as an intersite transition between a full and an empty e_g level, thereby representing a dynamic Jahn-Teller effect. The lower edge of the polaron absorption determines the activation energy of the activated DC conductivity and of the line width as observed in ESR experiments above $T_{\rm CO}$. Below the charge-order transition the DC transport closely follows the predictions of the VRH hopping model, *i.e.* at $T_{\rm CO}$ the transport mechanism seems to change from predominantly thermally activated to tunneling.

This research was supported by the Deutsche Forschungsgemeinschaft *via* the Sonderforschungsbereich 484 and by the BMBF *via* the contract number EKM 13N6917.

References

1. K. Chahara, T. Ohno, M. Kasai, Y. Kozono, Appl. Phys. Lett. **63**, 1990 (1993); R. von Helmolt, J. Wecker, B. Holzapfel, L. Schultz, K. Samwer, Phys. Rev. Lett. **71**, 2331 (1993); S. Jin, T.H. Tiefel, M. McCormack, R.A. Fastnacht, R. Ramesh, L.H. Chen, Science **264**, 413 (1994).
2. Y. Tomioka, A. Asamitsu, Y. Moritomo, Y. Tokura, J. Phys. Soc. Jpn **64**, 3626 (1995).
3. V. Kiryukhin, D. Casa, J.P. Hill, B. Keimer, A. Vigliante, Y. Tomioka, Y. Tokura, Nature **386**, 813 (1997).
4. K. Miyano, T. Tanaka, Y. Tomioka, Y. Tokura, Phys. Rev. Lett. **78**, 4257 (1997).
5. A. Asamitsu, Y. Tomioka, H. Kuwahara, Y. Tokura, Nature **388**, 50 (1997).
6. Z. Jirák, S. Krupička, V. Nekvasil, E. Pollert, G. Villeneuve, F. Zounová, J. Magn. Magn. Mater. **15-18**, 519 (1980).
7. E. Pollert, S. Krupička, E. Kuzmicova, J. Phys. Chem. Sol. **43**, 1137 (1982).
8. Z. Jirák, S. Krupička, Z. Šimša, M. Dlouhá, S. Vratislav, J. Magn. Magn. Mater. **53**, 153 (1985).
9. J.B. Goodenough, Phys. Rev. **100**, 564 (1955).
10. E.O. Wollan, W.C. Koehler, Phys. Rev. **100**, 545 (1955).
11. Y. Tomioka, A. Asamitsu, H. Kuwahara, Y. Moritomo, Phys. Rev. B **53**, R1689 (1996).
12. H. Yoshizawa, H. Kawano, Y. Tomioka, Y. Tokura, Phys. Rev. B **52**, R13145 (1995).

13. A. Anane, J.-P. Renard, L. Reversat, C. Dupas, P. Veillet, Phys. Rev. B **59**, 77 (1999)
14. Y. Morimoto, H. Kuwahara, Y. Tomioka, Y. Tokura, Phys. Rev. B **55**, 7549 (1997).
15. H. Yoshizawa, R. Kajimoto, H. Kawano, Y. Tomioka, Y. Tokura, Phys. Rev. B **55**, 2729 (1997).
16. D.E. Cox, P.G. Radaelli, M. Marezio, S.-W. Cheong, Phys. Rev. B **57**, 3305 (1998).
17. A. Moreo, S. Yunoki, E. Dagotto, Science **283**, 2034 (1999).
18. Y. Okimoto, Y. Tomioka, Y. Onose, Y. Otsuka, Y. Tokura, Phys. Rev. B **57**, R9377 (1998).
19. Y. Okimoto, Y. Tomioka, Y. Onose, Y. Otsuka, Y. Tokura, Phys. Rev. B **59**, 7401 (1999).
20. U. Schneider, P. Lunkenheimer, A. Pimenov, R. Brand, A. Loidl, Ferroelectrics (in press), `cond-mat/9908279`.
21. A.A. Volkov, Yu.G. Goncharov, G.V. Kozlov, S.P. Lebedev, A.M. Prokhorov, Infrared Phys. **25**, 369 (1985); A.A. Volkov, G.V. Kozlov, S.P. Lebedev, A.M. Prokhorov, Infrared Phys. **29**, 747 (1989); G.V. Kozlov, A.A. Volkov, in *Millimeter and Submillimeter Wave Spectroscopy of Solids*, edited by G. Grüner (Springer, Berlin, 1998), p. 51.
22. J.H. Jung, K.H. Kim, D.J. Eom, T.W. Noh, E.J. Choi, J. Yu, Y.S. Kwon, Y. Chung, Phys. Rev. B **55**, 15489 (1997).
23. Y. Tomioka, H. Kuwahara, A. Asamitsu, T. Kimura, R. Kumai, Y. Tokura, Physica B **246-247**, 135 (1998).
24. R. Kajimoto, T. Kakeshita, Y. Oohara, H. Yoshizawa, Y. Tomioka, Y. Tokura, Physica B **241-243**, 436 (1997).
25. J. Fontcuberta, B. Martinez, A. Seffar, S. Pinol, J.L. Garcia-Muños, X. Obradors, Phys. Rev. Lett. **76**, 1122 (1996); M. Paraskevopoulos, F. Mayr, J. Hemberger, A. Loidl, R. Heichele, D. Maurer, V. Müller, A.A. Mukhin, A.M. Balbashov, J. Phys. Cond. Matt. **12**, 3993 (2000).
26. M.R. Lees, O.A. Petrenko, G. Balakrishnan, D. McK. Paul, Phys. Rev. B **59**, 1298 (1999).
27. A.P. Ramirez, P. Schiffer, S-W. Cheong, C.H. Chen, W. Bao, T.T.M. Palstra, P.L. Gammel, D.J. Bishop, B. Zegarski, Phys. Rev. Lett. **76**, 3188 (1996).
28. P. Lunkenheimer, J. Sichelschmidt, F. Mayr, A. Pimenov, K. Pucher, J. Hemberger, A.A. Mukhin, A.M. Balbashov, A. Loidl (to be published).
29. P. Lunkenheimer, M. Resch, A. Loidl, Y. Hidaka, Phys. Rev. Lett. **69**, 498 (1992); M. Dumm, P. Lunkenheimer, A. Loidl, B. Assmann, H. Homborg, P. Fulde, J. Chem. Phys. **104**, 5048 (1996).
30. A. Seeger, P. Lunkenheimer, J. Hemberger, A.A. Mukhin, V.Yu. Ivanov, A.M. Balbashov, A. Loidl, J. Phys. Cond. Matt. **11**, 3273 (1999).
31. A.K. Jonscher, *Dielectric Relaxation in Solids* (Chelsea Dielectrics Press, London, 1983); A.K. Jonscher, *Universal Relaxation Law* (Chelsea Dielectrics Press, London, 1996).
32. W.K. Lee, J.F. Liu, A.S. Nowick, Phys. Rev. Lett. **67**, 1559 (1991); A.S. Nowick, A.V. Vaysleyb, B.S. Lim, J. Appl. Phys. **76**, 4429 (1994).
33. M. Dumm, M. Dressel, M. Nicklas, P. Lunkenheimer, A. Loidl, M. Weiden, F. Steglich, B. Assmann, H. Homborg, P. Fulde, Euro. Phys. J. B **6**, 317 (1998).
34. S.R. Elliott, Solid State Ionics **70/71**, 27 (1994); D.L. Sidebottom, P.F. Green, R.K. Brow, J. Non-Cryst. Solids **203**, 300 (1995); K.L. Ngai, H. Jain, O. Kanert, J. Non-Cryst. Solids **222**, 383 (1997).
35. D.L. Sidebottom, P.F. Green, R.K. Brow, Phys. Rev. Lett. **74**, 5068 (1995).
36. see, *e.g.*, A.R. Long, Adv. Phys. **31**, 553 (1982); S.R. Elliott, Adv. Phys. **36**, 135 (1987).
37. A.J. Millis, R. Mueller, B.I. Shraiman, Phys. Rev. B **54**, 5405 (1996).
38. M. Quijada, J. Cerne, J.R. Simpson, H.D. Drew, K.H. Ahn, A.J. Millis, R. Shreekala, R. Ramesh, M. Rajeswari, T. Venkatesan, Phys. Rev. B **58**, 16093 (1998).
39. D. Emin, Phys. Rev. B **48**, 13691 (1993).
40. W.G. Fateley, N.T. McDevitt, F.F. Bentley, Appl. Spectrosc. **25**, 155 (1971).
41. G. Feher, A.F. Kip, Phys. Rev. **98**, 337 (1955).
42. V.A. Ivanshin, J. Deisenhofer, H.-A. Krug von Nidda, A.A. Mukhin, A.M. Balbashov, Phys. Rev. B **61**, 6213 (2000).
43. D. Emin, Ann. Phys. **53**, 439 (1969).
44. A. Shengelaya, G. Zhao, H. Keller, K.A. Müller, B.I. Kochelaev, Phys. Rev. B **61**, 5888 (2000).
45. J. Sichelschmidt, B. Elschner, A. Loidl, B.I. Kochelaev, Phys. Rev. B **51**, (1995) 9199.